DE GRUYTER e-Polymers 2025; 25: 20250043

Research Article

Yu-Chang Huang, Po-Hao Tseng, Yen-Zen Wang*, Ko-Shan Ho*, Yan-Cheng Lin, and Che-Ju Tseng

Metal-free N, S-co-doped carbon materials derived from calcined aromatic co-poly(urea-thiourea)s as efficient alkaline oxygen reduction catalysts

https://doi.org/10.1515/epoly-2025-0043
received July 01, 2025; accepted August 15, 2025

Abstract: This study presents a sustainable strategy for the development of metal-free electrocatalysts derived from degraded aromatic co-poly(urea-thiourea)s. Upon pyrolysis under a nitrogen atmosphere, the polymers are transformed into N, S-co-doped turbostratic carbon nanomaterials with a high specific surface area exceeding 1,000 $m^2 \cdot g^{-1}$ and an optimized electronic structure. The resulting materials exhibit outstanding electrocatalytic performance in the oxygen reduction reaction (ORR), characterized by a high onset potential (0.96 V), half-wave potential (0.82 V), large limiting current density ($-6.21\ mA \cdot cm^{-2}$), and a low Tafel slope ($87.6\ mV \cdot dec^{-1}$). The number of electrons transferred during ORR is close to 3.9, approaching the ideal four-electron pathway. The material delivers a maximum power density of $443.8\ mW \cdot cm^{-2}$, outperforming that of commercial Pt/C.

Keywords: metal-free, carbon materials, alkaline catalyst, oxygen reduction reaction

1 Introduction

The challenge of acid etching remains a persistent issue for metal catalysts in proton exchange membrane fuel cells due to their acidic operating environment. Transitioning to an alkaline system, such as anion exchange membrane fuel cells (AEMFCs), may mitigate oxidation concerns.

Currently, platinum–carbon (Pt/C) catalysts are the only successfully commercialized catalysts for AEMFCs. However, Pt/C catalysts suffer from several inherent drawbacks, including carbon monoxide poisoning, poor methanol tolerance, long-term instability, and high cost. These limitations significantly impede the advancement of AEMFC technology. Various research approaches have been explored to reduce catalyst costs, including replacing Pt with low-cost transition metals in non-precious metal catalysts and developing nonmetallic catalysts by incorporating heteroatoms into the carbon matrix. While non-precious metal catalysts offer a balance between efficiency and cost, transition metals tend to aggregate under high-temperature sintering conditions, resulting in uneven catalytic activity. Additionally, the disposal of metal-based catalysts raises environmental concerns. Therefore, the necessity of recycling metal-containing catalysts remains. These challenges could be addressed through the development of metal-free catalysts for AEMFCs.

The main part of electrode catalysts is a conductive carbon matrix, which also needs to behave as an oxygen absorber to conduct the redox reactions. However, it lacks the polarity required to efficiently catalyze the oxygen reduction reaction (ORR) as the cathode catalysts on a large scale. This limitation, however, can be overcome by doping the carbon matrix with more electronegative atoms to introduce the necessary polarity.

Besides improving the polarity of the catalyst's carbon matrix, other physical properties are crucial for enabling metal-free carbon-based materials to serve as promising cathode catalysts. These include a high surface area and

---

*** Corresponding author: Yen-Zen Wang,** Department of Chemical and Materials Engineering, National Yunlin University of Science and Technology, 123, Section 3, University Road., Dou-Liu City, Yun-Lin, 64301, Taiwan, e-mail: wangzen@yuntech.edu.tw
*** Corresponding author: Ko-Shan Ho,** Department of Chemical and Materials Engineering, National Kaohsiung University of Science and Technology, 415, Chien-Kuo Road, Kaohsiung, 80782, Taiwan, e-mail: hks@nkust.edu.tw
Yu-Chang Huang, Yan-Cheng Lin, Che-Ju Tseng: Department of Chemical and Materials Engineering, National Kaohsiung University of Science and Technology, 415, Chien-Kuo Road, Kaohsiung, 80782, Taiwan
Po-Hao Tseng: School of Electrical and Electronics Engineering, Nanyang Technological University, 50 Nanyang Ave., Singapore, 639798, Singapore

appropriately sized pores to accommodate absorbed oxygen. However, obtaining carbon catalysts with a high surface area and abundant micropores from conductive carbon matrices such as carbon nanotubes (CNTs), graphenes (GFs), or graphene oxides is particularly challenging due to their well-defined structures. Such modifications typically require treatment with strong acids or highly reactive chemicals at high temperatures. Furthermore, doping highly conjugated structures like CNTs or GF with heteroatoms of high polarity can only be achieved through high-temperature calcination under harsh conditions (1–7).

Metal-free catalysts of carbonaceous materials calcined at high temperatures have attracted significant attention as environmentally friendly electrochemical catalysts, especially for their high electrical conductivity and electrochemical stability. They exhibit ORR activity comparable to or surpassing their metal-containing counterparts (8), making them a highly competitive alternative for ORR applications. The ORR mechanism involves the reduction of oxygen molecules that are adsorbed onto the carbon framework.

Among the carbon-based catalysts, polymer-derived carbon (PDC) precursors are a promising class of materials synthesized from calcined organic polymer precursors. It transforms long polymer chains into carbon materials via dehydration, cyclization, cross-linking, and carbonization. PDCs offer high design flexibility, allowing for precise compositional control and the facile incorporation of heteroatoms (9). The high cross-linking density or aromaticity of PDCs can enhance the final catalyst yield and conductivity. The thermal decomposition of the polymer also promotes the formation of a desirable porous structure. For example, Xing et al. (10) developed a yolk–shell nanostructure by calcining polyaniline@SiO_2 particles and etching the silica template. Such an approach formed a well-preserved nanostructure with mesopores and effective oxygen doping, significantly boosting catalytic activity. The specific properties of PDCs, including their tunable structure and composition, have provided widespread applications in energy storage, particularly for ORR catalysis. Common polymer precursors include polyaniline (10,11), polypyrrole (12,13), and polyimide (14). However, PDCs have limitations; some precursors can be complex to synthesize, exhibit low carbon yields, or are prone to structural collapse during processing.

Heteroatoms like N, S, and co-doping are common strategies to improve catalytic performance further. Palm et al. (15) prepared N, S co-doped nanocarbon composites based on silicon carbide-derived carbon, CNTs, and mesoporous carbon for ORR in anion-exchange membrane fuel cells (AEMFCs). Their best catalyst achieved a peak power density of 379 $mW{\cdot}cm^{-2}$, comparable to the performance of a commercial Pt/C catalyst (347 $mW{\cdot}cm^{-2}$). Similarly, Gong et al. (16) demonstrated that vertically aligned nitrogen-containing carbon nanotubes (VA-NCNTs) can be a superior metal-free electrode, revealing enhanced methanol crossover effects compared to platinum in alkaline fuel cells. These studies suggest that doping heteroatoms, such as nitrogen and sulfur, into the carbon framework, as in this work, plays a crucial role. These heteroatoms, which have an electronegativity compared to carbon, alter the local charge distribution of the carbon framework (16), which in turn enhances the adsorption of oxygen molecules and accelerates the ORR.

An approach to increase the porosity of the carbon-based catalysts and improve the capability of catalysis can be fulfilled by a thermal gas generator, ammonium chloride (NH_4Cl), which can be mixed with the polymer precursors (17–19) to release NH_3 and HCl gases during calcination to enhance the surface porosity. It can gradually decompose to produce a significant amount of mixed gases of NH_3 and HCl at around 350°C to further expand the carbon matrix. Thermally evolved ammonia is also a nitrogen dopant that increases the nitrogen content in the resulting materials. Additionally, the large molecular structure of ammonia and the gas expansion resulting from the decomposition of NH_4Cl generate substantial internal stress, acting as a pore-forming agent. Such an approach successfully fabricated graphite carbon materials with high specific surface areas and elevated nitrogen content. Furthermore, releasing small gas molecules, such as NH_3, H_2O, and H_2S, during the calcination of co-poly (urea-thiourea)s (PUTrs) can facilitate the formation of tiny pores in the catalyst, enhancing its surface area.

In this study, we synthesized aromatic PUTrs with a high density of aromatic units as precursors. Upon calcination in an N_2 atmosphere, these polymers undergo thermal degradation or crosslinking, forming a graphene-like (GF-like) conductive structure. Specifically, thermal degradation (calcination) increases porosity by generating new surface area by releasing small gas molecules such as NH_3, H_2O, and H_2S. Meanwhile, crosslinking reactions between intra- or intermolecular aromatic units in PUTr molecules contribute to forming highly conductive GF-like surfaces. Since direct heteroatom implantation onto a graphene-like surface is challenging, we developed aromatic sulfur-containing polyurea (PUr) polymers with two nitrogen atoms per urea unit (–NH–CS–NH–) as catalyst precursors. This approach enabled the synthesis of N, S co-doped GF-like carbonaceous catalysts for AEMFCs. Furthermore, by performing calcination in the presence of NH_4Cl, we successfully synthesized a metal-free, N, S co-doped conductive carbon substrate with an exceptionally high surface area and excellent catalytic activity for the ORR.

2 Materials and methods

2.1 Preparation of metal-free nitrogen-doped cathode catalyst (MFNCC)

Based on a molar ratio of 1.25:1, 0.685 g of *p*-phenylenediamine (PDA) and 0.8 g of *p*-phenylene isocyanate (PDI) are placed separately in beakers with 50 mL of acetone as the solvent. The individual solutions are subjected to 15 min of ultrasonic agitation before mixing. Subsequently, the solutions are mixed and heated to 70°C under vigorous magnetic stirring, and a gel-like substance gradually forms after a few seconds. The reaction is allowed to proceed at room temperature for 6 h. Vacuum filtration is then performed, and the products are washed with abundant acetone several times to remove unreacted monomers and are vacuum-dried at 70°C for 12 h to obtain the catalyst precursor (PUr).

The catalyst precursor (PUr) was then finely ground into powders, and equal amounts of powders (1.0 g) and NH_4Cl (1.0 g) were mixed thoroughly in an agitator. The mixture was placed in a ceramic crucible, and a tube furnace was purged with a high-purity nitrogen atmosphere. The temperature was increased to 1,000°C at $10°C{\cdot}min^{-1}$, holding at 1,000°C for 30 min. Once the sample was cooled to room temperature, the preparation of the nitrogen-doped catalyst was complete (Figure S1).

2.2 Preparation of nitrogen, sulfur-co-doped carbon catalyst

The preparation of N, S-co-doped carbon catalyst follows a procedure similar to that described in the above section, except that 0.96 g of *p*-phenylene diisothiocyanate was mixed with 1 g of PDI before the polymerization, and the obtained precursor polymer is named as PUTr (polyurea-thiourea).

2.3 Electrochemical measurements

2.3.1 Preparation of catalyst ink for cyclic voltammetry (CV) and linear sweep voltammetry (LSV)

Catalyst ink is prepared by mixing 2.9 mg of the catalyst with 357 μL of deionized water, 357 μL of ethanol as the solvent, and 7.2 μL of a 20% Nafion solution. The mixture is then subjected to ultrasonic treatment for at least 1 h to complete the ink preparation.

2.3.2 LSV analyses

The LSV tests were conducted using an AutoLab system in a 0.1 M KOH solution saturated with oxygen. To prepare for the test, 5 μL of the catalyst ink was repeatedly drop-casted and dried onto a glassy carbon working electrode, ensuring complete coverage. The working electrode was then mounted on a rotating disk electrode (RDE). A platinum wire served as the counter electrode, and an Ag/AgCl electrode was used as the reference electrode. The testing conditions involved a scan rate of $5\ m{\cdot}V^{-1}$, rotation speeds ranging from 400 to 2,500 rpm, and a potential range from 1.2 to 0 V (vs reversible hydrogen electrode [RHE]). The setup for the LSV tests at different rotation speeds is illustrated in Figure S2.

2.3.3 RRDE measurements

RRDE measurements were conducted using a CHI three-electrode electrochemical workstation in a 0.1 M KOH solution (200 mL) saturated with oxygen. In all, 14.4 μL of the slurry prepared in Section 2.3.1 was drop-cast onto a glassy carbon electrode in multiple layers and dried. A platinum wire was used as the counter electrode, while an Hg/HgO electrode was the reference electrode. The ring potential was maintained at 0.5 V (vs Hg/HgO), with a rotation speed of 1,600 rpm. The potential was scanned from 0.1 to 0.3 V (vs Hg/HgO) at $5\ mV{\cdot}s^{-1}$ scan rate.

2.3.4 CV analyses

The CV analyses were conducted using an AutoLab system in a 0.1 M KOH solution, saturated with oxygen and nitrogen. These tests were performed without applying a rotation speed. The potential was scanned from 1.2 to 0 V (vs RHE), with a scan rate of $50\ mV{\cdot}s^{-1}$. The experimental setup for CV tests was consistent with Figure S2.

2.3.5 Durability testing

The durability of the catalyst was evaluated using chronoamperometry, carried out in a 0.1 M KOH solution saturated with oxygen. During a 25,000 s run, the system was maintained at a constant rotational speed of 1,200 rpm and a fixed potential of 0.5 V (vs RHE). This test was performed to observe how the current density changed over time under these specific conditions.

To assess methanol tolerance, at 300 s into the test, 3 M methanol solution was introduced to the system to monitor its performance in the presence of methanol.

2.3.6 Membrane electrode assembly (MEA) fabrication

2.3.6.1 Membrane pre-treatment

The X37-50RT anion exchange membrane was immersed in a 1 M KOH solution for 48–72 h to activate it, ensuring its complete transformation into the OH^- form. The activated membrane was then stored in 1 M KOH for future use.

2.3.6.2 Catalyst ink for MEA

The anode employed a Pt/C catalyst with an anode loading of 0.8 mg Pt cm^{-2}. The cathode used catalysts, including NCs and NCSs, with a cathode loading of 3.5 mg·cm^{-2} for this experiment. A total of 9 mg of Pt/C catalyst and 7.875 mg of the cathode catalyst for this experiment were separately weighed into sample vials. Subsequently, 400 mg of DI water and 400 mg of isopropanol were added and subjected to 30 min of ultrasonication. Then, 90 mg of XB-7 alkaline ionomer was mixed in, and ultrasonication was continued for 90 min until the powder was completely dispersed, resulting in a uniform black ink.

2.3.7 Assembly of single-cell components

The components are assembled into an MEA using a sandwich structure, and it is placed in the center of the single-cell component. A torque wrench is used to compress the components at 8 kgf·cm^{-2}, ensuring even force application diagonally to complete the component assembly (Figure S3).

2.3.8 Analyses of single cell

The anode and cathode of the component are connected to the gas inlet and outlet pipes to ensure there is no gas

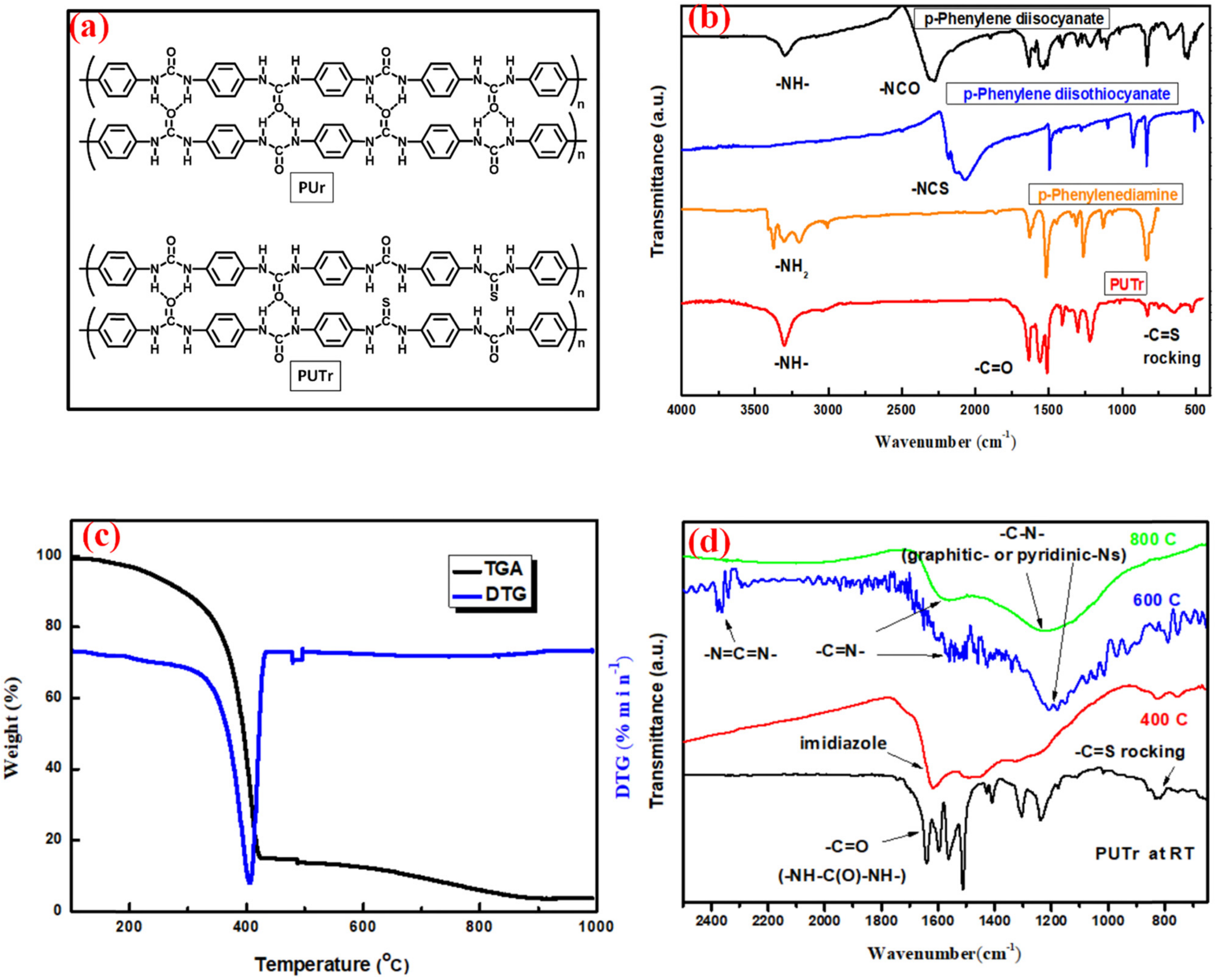

Figure 1: (a) Intermolecular H-bonding of PUr and PUTr, (b) IR spectra of monomers and PUTr, (c) TGA and DTG thermograms of PUTr, and (d) IR spectra of PUTr measured at various calcination temperatures.

leakage and to prevent any hazards. The polarization curve measurement is then conducted to obtain the open-circuit voltage (OCV) and power density from the actual operating fuel cell. The operating parameters for single testing are listed in Table S1.

3 Results and discussion

3.1 Characterization

Aromatic PUrs were synthesized via the condensation polymerization of PDA with either PDI or *p*-phenylene diisothiocyanate, as illustrated in Figure S4. The resulting polymers feature a regular, alternating sequence of urea and phenylene units, facilitating extensive, ordered intermolecular hydrogen bonding (Figure 1(a)).

The functional groups of both monomers and polymer intermediates were confirmed by Fourier-transform infrared (FTIR) spectroscopy (Figure 1(b)). In the spectra of the PUr precursors, the characteristic isocyanate (–N═C═O) stretching band at 2,274 cm^{-1} and the isothiocyanate (–N═C═S) band at 2,059 cm^{-1} disappear completely, indicating complete conversion of the diisocyanate and diisothiocyanate reactants. Concurrently, the primary amine signals of PDA (–NH_2) in the 3,300–3,500 cm^{-1} region diminish, replaced by secondary amine vibrations in the polymer. The appearance of aromatic C═C stretching at 1,512 cm^{-1} and the urea C═O band at 1,636 cm^{-1} further corroborates the successful formation of aromatic PUrs (20).

Moreover, the hydrogen-bonding environment within the polymer matrix is evidenced by the redshift of the N–H stretching band from 3,450 cm^{-1} (free) to 3,413 cm^{-1}, and of the C═O stretching band from 1,690 cm^{-1} (free) to 1,636 cm^{-1}. These shifts reflect the establishment of a robust, ordered hydrogen-bond network, which also accounts for the gel-like character of the as-prepared PUrs.

Thermogravimetric analyses under an inert atmosphere reveal a multistage thermal decomposition profile for the PUr derived from PDA and PDI (PUTr) (Figure 1(c)). In the initial stage (300–600°C), cleavage of urea (–NH–CO–NH–) and thiourea (–NH–CS–NH–) linkages yields isocyanate/isothiocyanate species, amines, and carbodiimide (–N═C═N–) intermediates (21–24), accompanied by the evolution of small gaseous molecules such as H_2O, NH_3, CO_2, and H_2S (Figure S5). The resulting aromatic fragments, enriched in reactive functional groups, undergo cyclization and condensation upon further heating (600–800°C), leading to sulfur-doped polycyclic aromatic hydrocarbons, including thiophene and thiazole moieties (Figure S6). These transformations enhance the material's conjugation and electrical conductivity while retaining nitrogen and sulfur heteroatoms for catalytic activity. At higher temperatures (800–1,000°C), extensive condensation drives graphitization and the formation of graphene-like domains (Figure S7), with residual N and S atoms embedded within the carbon lattice, thereby augmenting

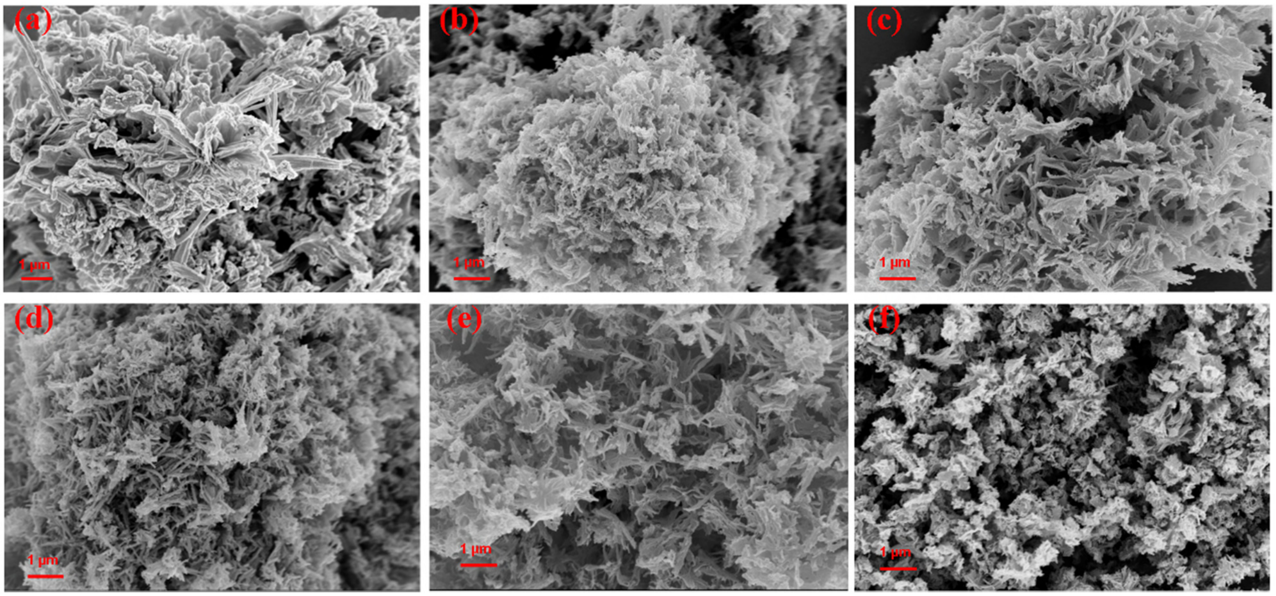

Figure 2: SEM micrographs of (a) PUTr, (b) NC-800, (c) NC-900, (d) NC-1000, (e) NC-100N, and (f) NCS-1000N.

the electronic and catalytic properties of the carbonized product.

The proposed degradation mechanisms were further elucidated by *in situ* FTIR analyses of samples calcined at incremental temperatures (Figure 1(d)). Initial cleavage reactions generate aromatic isocyanate and amine fragments, followed by the formation of carbodiimide functionalities. Between 600°C and 800°C, biuret–imine units reorganize into reactive N═C═N-containing carbodiimide intermediates, which facilitate additional cyclization and cross-linking reactions. These observations reveal that the thermal degradation of aromatic PUrs proceeds through an interconnected network of bond scission, rearrangement, and aromatization reactions, culminating in heteroatom-doped carbonaceous frameworks (Figures S5–S7).

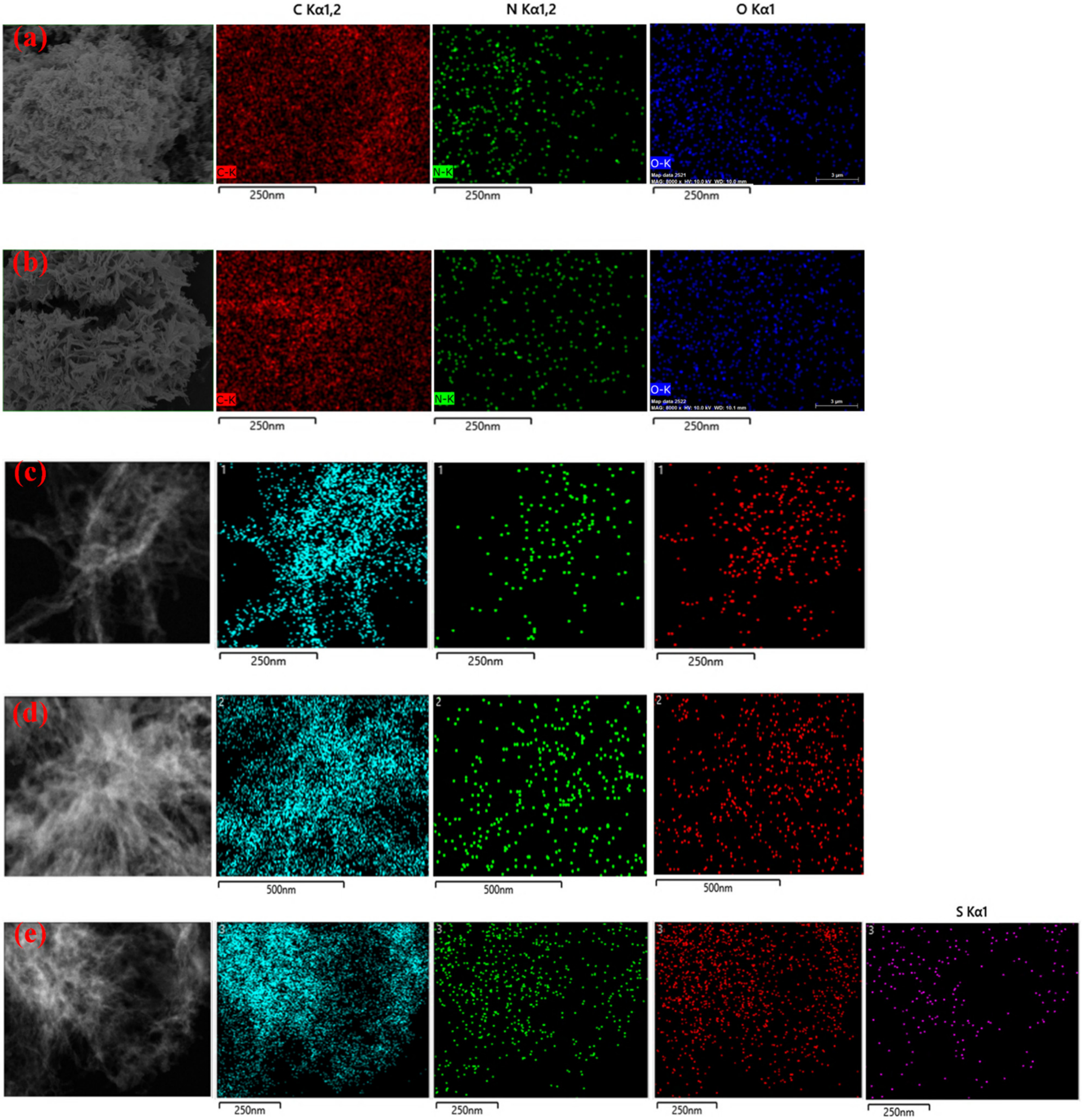

Figure 3: EDs of C, N, O, and S mappings in (a) NC-800, (b) NC-900, (c) NC-1000, (d) NC-1000N, and (e) NCS-1000N.

3.2 Scanning electron microscopy (SEM)

As shown in Figure 2(a), the initially compact, block-like precursor aggregates (PUTr) undergo high-temperature pyrolysis and transform into two-dimensional, rose-like creation of the nanosheets (25) due to the strong hydrogen-bonding interactions within the aromatic PUr framework (26). Such ultra-thin nanosheets facilitate superior electrical conductivity and reduce ohmic polarization. Some of the aggregated polymer molecules by H-bonding even convert to nanofibers after calcination, as seen in Figure 2(b)–(f).

According to the TGA results, no additional weight loss occurs above 900°C, indicating that N-containing segments generated from PUTr decomposition and pores formed by small molecule release are primarily responsible for the structural changes. Consequently, NC-900 (Figure 2(c)) and NC-1000 (Figure 2(d)) exhibit more porous architectures than NC-800 (Figure 2(b)). As the pyrolysis temperature increases, the carbon framework experiences more significant disruption, resulting in a defect-rich structure in NC-1000 that suggests a higher specific surface area. Figure 2(e) demonstrates the effect of NH_4Cl-assisted pyrolysis on the carbon morphology. The decomposition of NH_4Cl releases substantial ammonia gas, whose relatively large molecules induce further pore formation. This process produces a more fractured microstructure in NC-1000N compared to NC-1000, rendering it markedly different from the original PU precursor, which agrees with transmission electron microscopy (TEM) observations. The newly formed pores increase the specific surface area. In contrast, the high degree of graphitization and expanded surface area in NC-1000N confer excellent electrical conductivity and oxygen mass-transfer capabilities, enhancing oxygen diffusion and improving the overall current density reduction. Eventually, the SEM image of the N, S co-doped catalyst (Figure 2(f)) shows that NCS-1000N and NC-1000N share similar porous surface morphologies. However, compared to TEM analyses, the sulfur-induced defects in the graphene-like carbon nanosheets are not as significant in the SEM micrographs. Further investigation based on BET analyses is necessary to clarify the porous characteristics of these materials.

Energy-dispersive X-ray spectroscopy mapping was employed to investigate the elemental distribution and composition of the catalysts, as presented in Figure 3. The quantitative elemental compositions of each sample are summarized in Table 1. The catalysts were synthesized under varying conditions, including different calcination temperatures (Figure 3(a)–(c)), the presence of NH_4Cl (Figure 3(d)), and sulfur doping (Figure 3(e)). The EDs mapping results demonstrate a uniform distribution of carbon (C), nitrogen (N), and oxygen (O) across all samples, indicating the absence of metal catalyst agglomeration. As the calcination temperature increases, an enhancement in the graphitization degree of the carbon framework is evident, with the NC-1000 sample exhibiting the highest carbon content (86.76%), as shown in Table 1.

Table 1: Element analyses of various NCs

	NCs				
Element	**NC-800**	**NC-900**	**NC-1000**	**NC-1000N**	**NCS-1000N**
C	76.18	78.88	86.76	78.29	85.99
N	10.43	8.14	7.01	7.53	3.5
O	13.39	12.97	6.23	14.18	10.24
S	—	—	—	—	0.28

Moreover, the effect of the second nitrogen doping via NH_4Cl treatment is apparent in the NC-1000N sample, which shows a relatively higher nitrogen content (7.53%) compared to NC-1000 (7.01%). It means that NH_4Cl can practically supply nitrogen loss at elevated temperatures, preserving active nitrogen sites while maintaining electrical conductivity, which are factors essential for improved catalytic performance.

Besides, the elemental mapping of the NCS-1000N illustrates successful sulfur doping into the carbon matrix, as indicated by the presence of S signals in Figure 3(e). It verifies the effective synthesis of N, S-co-doped carbon materials, supporting the feasibility of the designed doping strategy.

3.3 TEM

The pristine PUTr (Figure 4a) displays a flower-like morphology composed of fibrous, self-assembled bundles held together by hydrogen bonds. Upon heating, the release of H_2O and NH_3 disrupts these hydrogen bonds, driving cross-linking and conjugation into a robust, single-layer, graphene-like structure. As the calcination temperature approaches 1,000°C, π–π stacking between sheets leads to turbostratic fringes (Figure S8). The surface of the catalyst gradually evolves into a more porous, defect-rich network. Such transformation is primarily attributed to the evolution of gaseous byproducts such as H_2O, CO_2, and NH_3 during thermal decomposition (Figure 4(b)–(d)).

Figure 4(e) compares NC-1000 and NC-1000N, the latter synthesized with NH_4Cl as a pore-forming additive. During calcination, NH_4Cl decomposes to release NH_3 gas, thereby promoting the formation of additional porosity and increasing the density of electrochemically active sites. As observed in Figure 4(e), NC-1000N displays a more open and irregular microstructure than NC-1000, indicative of a higher surface area favorable for ORR activity.

Furthermore, the effect of sulfur doping on catalyst morphology was investigated through TEM analyses of NCS-1000N (Figure 4(f)). Previous studies have demonstrated that sulfur incorporation via C–S–C bonding introduces structural defects that can enhance catalytic performance (27,28). The TEM images reveal that sulfur doping results in a significantly rougher and more irregular surface (Figure 4(f)), suggesting an increase in specific surface area and improved mass transport properties, both beneficial for ORR performance.

To confirm the presence of turbostratic carbon – a structure typically observed in carbonaceous materials calcined at approximately 1,000°C – a high-resolution TEM image of NCS-1000N was obtained and is provided in Figure S9. The image reveals that turbostratic structures are prevalent throughout the material, consisting of multiple layers of graphene fragment clusters, which are known to exhibit high surface area and structural disorder advantageous for catalytic applications.

3.4 Structural analyses

Figure 5(a) presents the X-ray diffraction (XRD) patterns of the PUr precursor and various MFNCC materials synthesized under different processing conditions, serving as the basis for structural analyses. The Pur precursor exhibits sharp and well-defined diffraction peaks, which can be attributed to its fibrous structure, as shown in the top spectrum of Figure 5(a). In contrast, the diffraction patterns of the NC-series materials reveal prominent peaks at $2\theta = 25.5°$ and $2\theta = 43.8°$, corresponding to the (002) and (100) planes of graphitic carbon, respectively. These findings indicate that the calcination process effectively

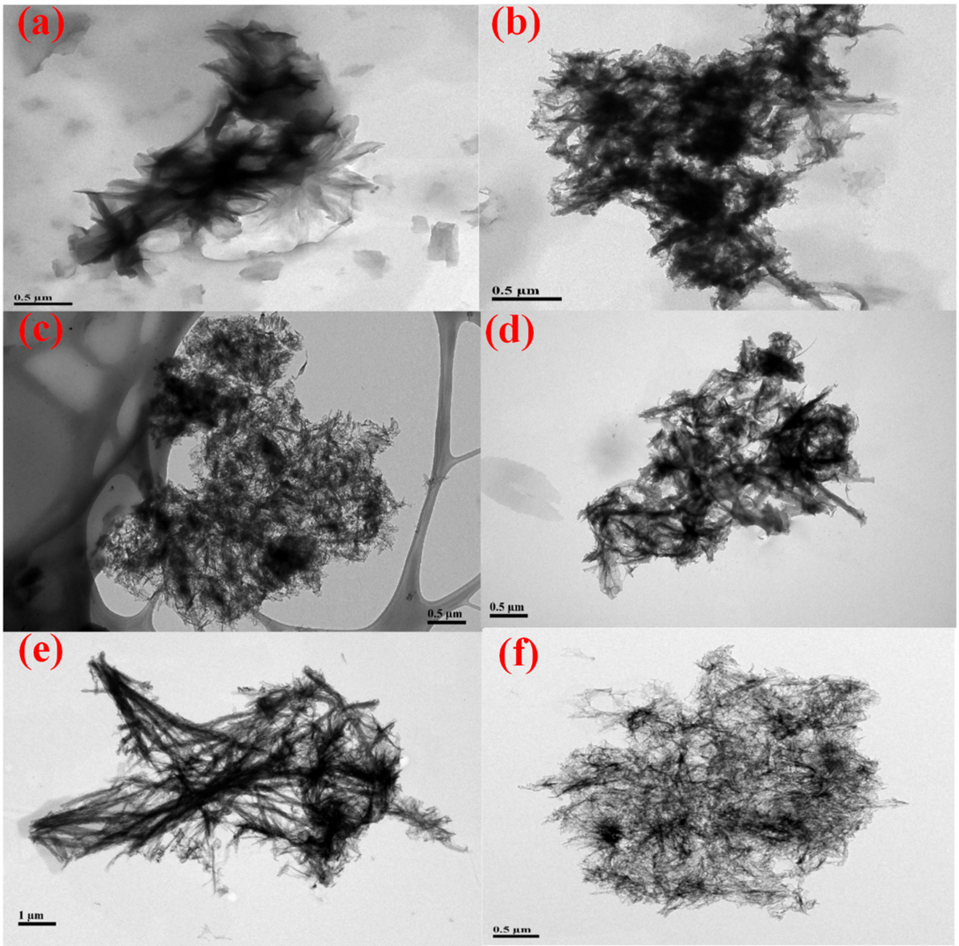

Figure 4: TEM micropictures of (a) PUr, (b) NC-800, (c) NC-900, (d) NC-1000, (e) NC-1000N, and (f) NCS-1000N.

converts the carbonaceous precursors into ordered graphitic structures, enhancing electrical conductivity.

Notably, the peak intensity at $2\theta = 43.8°$ increases significantly in the NC-1000, NC-1000N, and NCS-1000N samples following calcination at 1,000°C. As XRD peak intensity and sharpness indicate crystallinity, this enhancement suggests a higher degree of graphitization and a potentially increased graphene content. These structural improvements are expected to result in enhanced electrical conductivity, a hypothesis that subsequent performance evaluations will confirm, as more efficient charge transport pathways facilitate rapid electron transfer during electrocatalytic reactions.

Figure 5(b) shows the Raman spectra of the catalysts synthesized under varying calcination conditions, which were analyzed to assess lattice disorder and the degree of graphitization. The area ratios D (~1,350 cm^{-1}) and G bands (~1,590 cm^{-1}) are summarized in Table S2. As the calcination temperature increases from 800 to 1,000°C, the relative areas of the D band gradually decrease while that of the G band increases (Figure 5(c)). This trend reflects a reduction in structural disorder and sp^3-hybridized carbon defects, consistent with the thermal conversion of sp^3 carbon into more ordered sp^2-hybridized graphitic domains.

The G band, representing in-plane vibrational modes of sp^2-bonded carbon atoms, directly indicates graphitization. Its increased intensity at higher calcination temperatures confirms the improved structural ordering. However, the introduction of NH_4Cl as a pore generator, which decomposes to release NH_3 during calcination, disrupts the graphitic order. This disruption is evident from the increased D band areas and the decreased G band intensity in NC-1000N compared to NC-1000 (Figure 5I, Table S2). In contrast, sulfur doping in NCS-1000N does not significantly alter the relative band areas, suggesting minimal structural disruption.

Figure 5(d) and Table S2 further summarize the I_D/I_G intensity ratios for all NC samples, remaining less than one.

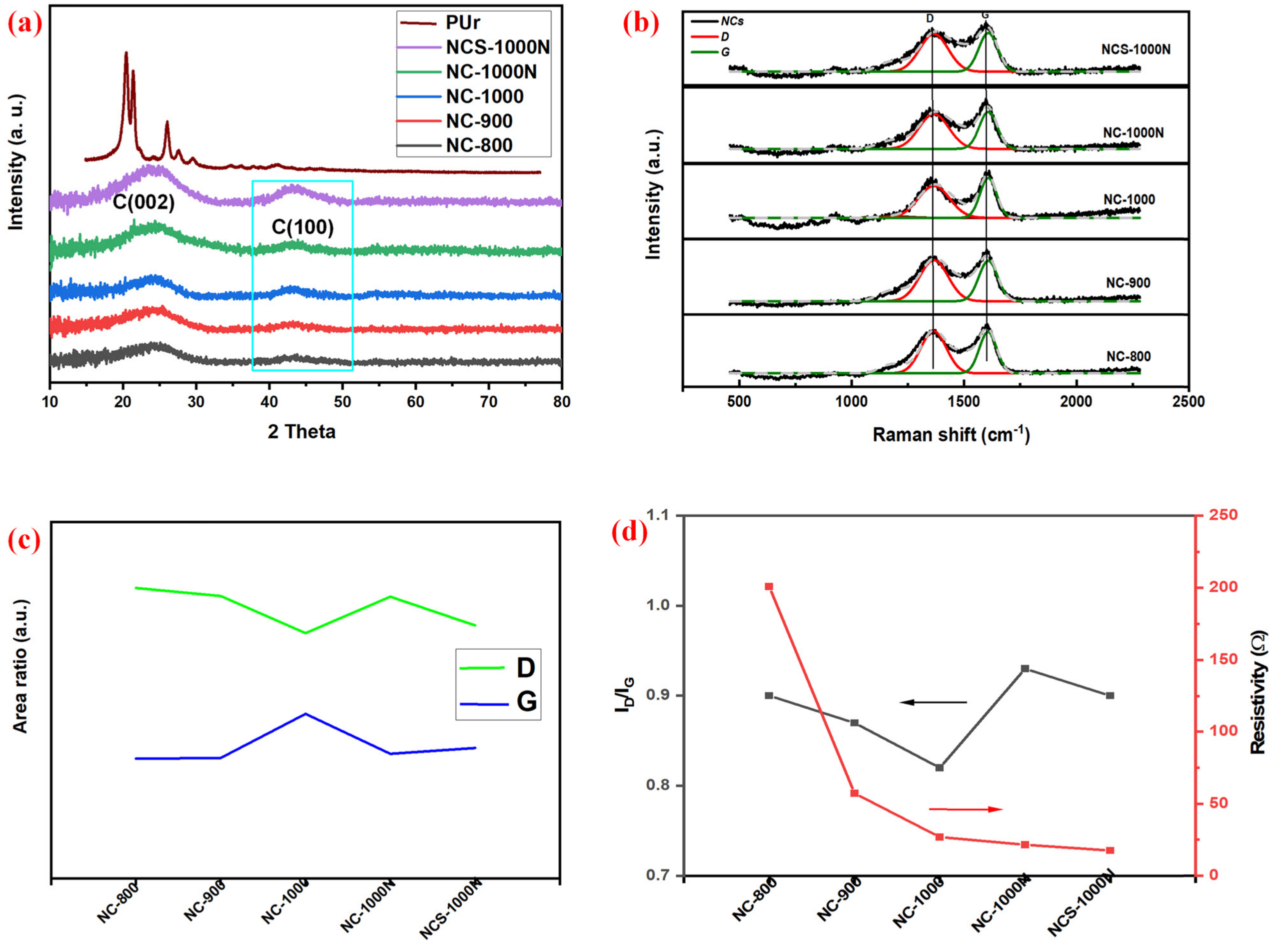

Figure 5: (a) X-ray diffraction patterns of PUr and various NCs, (b) Raman spectra of various NCs, (c) area ratios of various bands, and (d) I_D/I_G ratio and resistivity of various NCs.

It indicates that sp^2-hybridized carbon is predominant, and the materials are well graphitized. Interestingly, the I_D/I_G ratio initially decreases with increasing calcination temperature from 800 to 1,000°C in accordance with Table S2, reflecting the formation of more ordered graphite-like domains. However, in NC-1000N and NCS-1000N, the I_D/I_G ratio slightly increases. This increase can be attributed to the structural defects introduced by the gaseous byproducts from NH_4Cl decomposition and the heteroatom incorporation during sulfur doping.

These additional defects and the resultant increase in porosity contribute to a more disordered carbon structure. Such an increase in surface area shifts the catalyst towards a more disordered structure, increasing the intensity ratio. The affluent defects and pores can help facilitate the access of reactant gases to active sites, increasing the overall efficiency of active site utilization and improving the cell's power output.

3.5 Element analyses – X-ray Photoelectron Spectroscopy (XPS)

The catalyst's elemental properties and percentage content were analyzed using XPS to understand which type of nitrides can effectively promote the ORR. The high-resolution N_{1s} spectrum obtained from XPS can be fitted into four

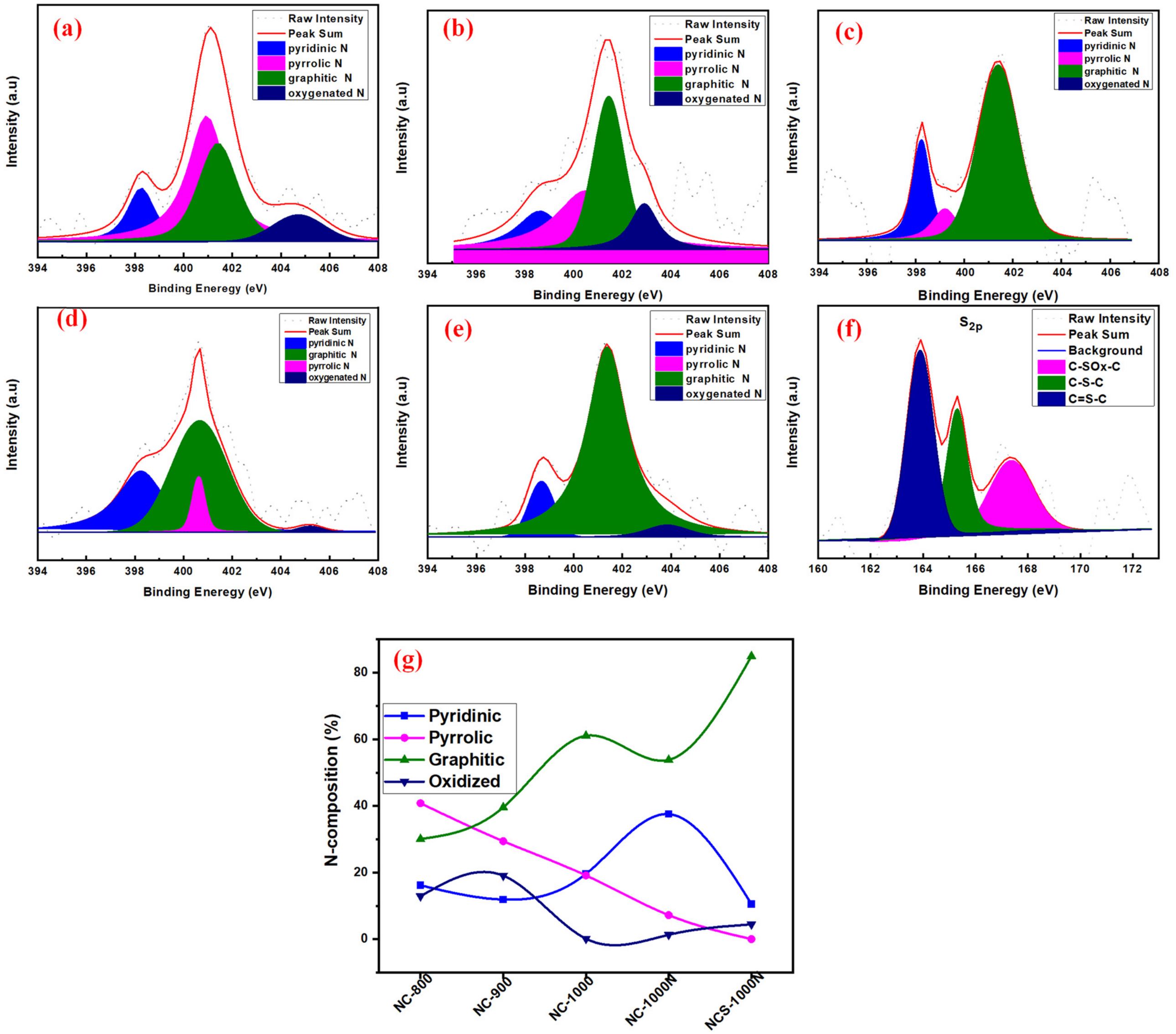

Figure 6: XPS of various NCs: N_{1s} of (a) NC-800, (b) NC-900, (c) NC-1000, (d) NC-1000N, (e) NCS-1000N; S_{2p} of (f) NCS-1000N and (g) various types of N-composition of different NCs.

different nitrogen species, including pyridinic-N (398.6 eV), pyrrolic-N (400.5 eV), graphitic-N (401.4 eV), and pyridine nitrogen oxide (402.0–405.0 eV), as illustrated in Figure S10.

Among these, pyridinic-N and graphitic-N are considered beneficial nitrogen species for catalysis (29,30). Pyridinic-N is bonded to two carbon atoms at the edges of graphene defects, providing an electron to the conjugated π-bond and possessing a pair of lone electrons, making it capable of attracting oxygen molecules for reactions (29). It can also promote an increase in the onset potential (31). Graphitic-N is found within the graphite plane, bonded to three carbon atoms, without lone electron pairs, and is more stable (30). It has a lower bandgap energy (32), which can enhance the desorption of neighboring carbon atoms and reduce the ORR activation energy (33), optimizing the limiting current density (31,34). In contrast, pyrrolic-N and pyridine-N oxide are generally considered to be nitrogen species without catalytic capabilities.

The deconvolution results reveal that NC-1000N and NCS-1000N are dominated by active configurations involving pyridinic-N and graphitic-N species, indicating the presence of the most abundant active site numbers. It can be inferred that they will exhibit superior electrochemical performance. Figure 6(a)–(e) displays the deconvolution results of the N_{1s} spectrum after sulfur doping. The results show a slight reduction in the pyridinic-N content while, in contrast, the content of graphitic-N has increased. Some literature suggests that sulfur co-doping alters the composition of nitrogen species. Sulfur co-doping tends to replace pyridinic-N located at the edges, resulting in a decrease in pyridinic-N content (35). It also leads to an enhancement in the overall content of graphitic-N, optimizing the catalyst's overall stability. Relevant studies have indicated that sulfur co-doping creates active sites at carbon atoms adjacent to graphitic-N, improving ORR performance (36).

S_{2p} can be deconvoluted into three peaks: thiophene-sulfur $2p_{3/2}$ (C=S–C; 164.0 eV), thiophene-sulfur $2p_{1/2}$ (C–S–C; 165.2 eV), and sulfur oxide ($C{-}SO_x{-}C$; 168.4 eV) (Figure 6(f)). The last column of Table 3S reveals that thiophene-sulfur species are predominant in NCS-1000N, confirming the presence of sulfur atoms doped into the carbon material. Sulfur-doped species have a significant impact on the positivity of the ORR. Prior literature suggests that thiophene-sulfur contributes to increasing the density of active catalytic sites (37) and improving the limiting diffusion current density of the ORR (38,39).

The results from Table S3 indicate that NCS-1000N has abundant pyridinic and graphitic-N species, with thiophene-sulfur species predominating. It suggests an excellent catalytic configuration; thus, NCS-1000N is expected to exhibit superior catalytic performance. As shown in Figure 6(g) and Table S3, it is evident that all the catalysts under different conditions exhibit favorable activity configurations with abundant pyridinic-N and graphitic-N content. Figure 6(g) and Table S3 indicate that the content of pyrrolic-N gradually decreases with increasing temperature. In contrast, the content of other active nitrogen species, pyridinic-N and graphitic-N, gradually increases. Such a phenomenon can be attributed to the decomposition of pyrrolic-N at 600°C, resulting in the formation of pyridinic-N, and with complete graphitization, temperatures exceeding 900°C lead to a gradual transformation into graphitic-N as an active nitrogen species.

3.6 ORR mechanism

Figure S11 illustrates the ORR pathways catalyzed by a metal-free, nitrogen-doped carbon catalyst involving both four-electron ($4e^-$) and two-electron ($2e^-$) mechanisms. In the $4e^-$ pathway (Figure S11(a), top), molecular oxygen (O_2) is first adsorbed onto the N-doped carbon active site, forming an adsorbed oxygen species stabilized via electron transfer from the conductive carbon matrix. It leads to the formation of a peroxide-like intermediate ($*O{-}O^-$), a strong base capable of abstracting hydrogen from water. The cleavage of the O–O bond then produces hydroxide ions (OH^-). The overall reaction can be summarized as:

$$O_2 + 2H_2O + 4e^- \rightarrow 4OH^-$$

This catalytic cycle begins with O_2 adsorption and electron transfer to yield the $*O{-}O^-$ species, which interacts with water to form *O–OH. This intermediate subsequently undergoes O–O bond cleavage upon further electron transfer, producing OH^- and leaving behind an *O species. This species is further reduced to *OH through additional hydrogen abstraction from water and electron acceptance. Finally, *OH is reduced to OH^-, regenerating the original active site and completing the catalytic cycle. This pathway ensures efficient oxygen reduction and high selectivity toward OH^- generation in alkaline conditions.

In contrast, the $2e^-$ pathway (Figure S11(b), bottom) represents a less desirable mechanism. Here, O_2 undergoes single-electron reduction to form the superoxide ($*O{-}O^-$), which extracts a hydrogen atom from water to form *O–OH. Rather than undergoing full O–O bond cleavage, the intermediate receives another electron and desorbs from the catalyst as hydroperoxide (HO_2^-), terminating the reaction prematurely:

$$O_2 + H_2O + 2e^- \rightarrow HO_2^- + OH^-$$

The partial reduction is unfavorable for fuel cell applications, as HO$_2^-$. It is known to degrade catalyst stability and reduce overall ORR efficiency. Therefore, improving the 4e$^-$ pathway is required for efficient energy conversion. The N-doped carbon catalyst facilitates this pathway by enabling efficient oxygen adsorption, activation, and electron transfer without metal-based active sites.

3.7 Surface property analyses (Brunauer–Emmett–Teller [BET])

The surface properties of the catalysts were characterized with nitrogen adsorption-desorption isotherms and BET analyses. All samples exhibit mesoporous structures, as defined by the IUPAC classification, and thus, the Barrett–Joyner–Halenda (BJH) method was applied to determine pore size distributions. The nitrogen adsorption–desorption isotherms of the synthesized catalysts display typical Type IV behavior with pronounced hysteresis loops, confirming their mesoporous nature. H3-type hysteresis loops indicate slit-like pores, typically associated with layered carbonaceous structures.

Figure 7(a) displays the BET surface area results for catalysts calcined at various temperatures. The NC-800 sample, obtained at the lowest calcination temperature, already demonstrates a high specific surface area of 676.47 m^2·g^{-1} due to the decomposition of thermally unstable urea units in the PU precursor, which release nitrogen-containing gases during pyrolysis. As the calcination temperature increases, the nitrogen adsorption capacity and the specific surface area increase significantly. It is attributed to enhanced decomposition of organic matter and the release of volatiles, such as water, up to 500°C. Consequently, the NC-1000 sample achieves a specific surface area of 997.10 m^2·g^{-1}, surpassing that of many reported N-doped carbon materials (Figure 7(a), Table 2).

Figure 7(b) compares the pore structures of catalysts prepared with and without NH$_4$Cl assistance at 1,000°C. NH$_4$Cl acts as a sacrificial template and pore-generator, releasing NH$_3$ and HCl gases during thermal decomposition. The evolution of these gases creates structural craters

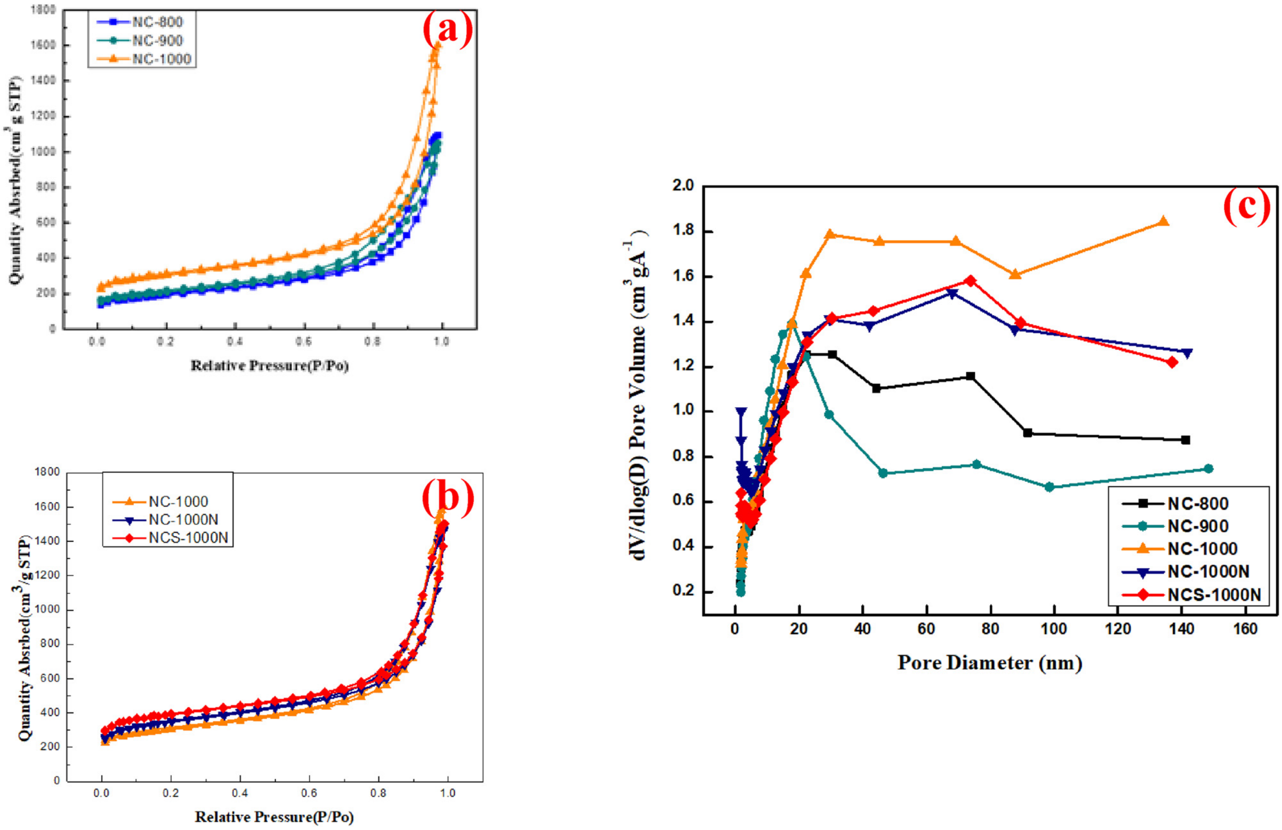

Figure 7: BET adsorption and desorption diagrams of (a) catalysts prepared at different temperatures, (b) different treatment catalysts prepared at 1,000°C, and (c) size distribution of various NCs.

and micropores within the carbon framework, particularly through the etching effect of the larger NH_3 molecules. As a result, the NC-1000N catalyst exhibits a significantly higher micropore surface area and reduced average pore size, yielding a BET surface area of 1,136.44 $m^2 \cdot g^{-1}$ (Table 2). This hierarchical pore structure improves the accessibility of active sites by facilitating oxygen diffusion through micropores, while mesopores enhance mass transport and product desorption, collectively boosting electrocatalytic activity (40).

Further surface analyses of sulfur- and nitrogen-co-doped carbon catalysts (Figure 7(b)) reveal that sulfur incorporation induces additional surface defects by bonding with carbon atoms in the graphitic plane. It increases disorder and contributes to further surface area enhancement. The resulting NCS-1000N sample exhibits the highest BET surface area of 1,256.67 $m^2 \cdot g^{-1}$, corroborating TEM observations of its well-developed, porous layered structure. The co-doping strategy, therefore, significantly amplifies porosity and surface complexity, which is favorable for ORR catalysis.

Combining the average pore sizes from Table 2 and the BJH pore size distribution profiles shown in Figure 7(c), it is evident that the catalysts primarily consist of mesoporous structures with embedded micropores. This hierarchical architecture is advantageous for fuel cell applications, as mesopores facilitate effective mass transport and water management. At the same time, micropores enhance active site exposure, which is critical for improving catalyst performance and operational longevity (41,42).

3.8 Electrochemical analyses

3.8.1 CV

Figure 8(a) reveals that, with an increase in material calcination temperature, the reduction peaks become more prominent, confirming that the reduction activity is directly proportional to the calcination temperature. The NC-1000N catalyst prepared with NH_4Cl as an assistive pore-forming agent exhibits a significantly more positive reduction peak position and higher current density than NC-1000. It demonstrates the successful strategy of using NH_4Cl as a pore-forming agent, significantly increasing the micro-pore area and enhancing the reducibility towards oxygen. The reduction peak position of the NCS-1000N catalyst is similar to that of NC-1000N. However, sulfur doping significantly increases the current intensity of the reduction peak, indicating that double-atom-doped catalysts have better mass transfer rates, slowing down concentration polarization and leading to increased current density. None of the catalysts exhibit significant current peaks in nitrogen, showing selectivity towards oxygen. The size of the CV curve area can be used to infer the relative surface area of the materials. Materials with higher surface areas typically have more pores, higher specific capacitance, and larger CV curve areas. The results in Figure 8(a) show that NCS-1000N has a larger CV curve area, consistent with the high surface area indicated by the BET results in Section 3.8.

3.8.2 LSV

Figure 8(b) shows that NC-1000 outperforms the catalysts calcined at the other two temperatures in all three regions: kinetic, mixed kinetics, and mass transport diffusion. Its excellent performance can be attributed to the complete graphitization level explained earlier in Section 3.5, which reduces Ohmic resistivity, resulting in higher conductivity and a more advanced $E_{1/2}$. This performance improvement is also supported by the TGA results in Section 3.1 and the BET results in Section 3.5. The pyrolysis condition at 1000°C allows for the complete release of urea units and water molecules from the precursor, optimizing its surface area and improving the diffusion current density of NC-1000.

Table 2: BET analyses of various cathode catalysts obtained from the N_2 adsorption–desorption curves

Cathode catalysts	BET surface area ($m^2 \cdot g^{-1}$)	Micropore surface area ($m^2 \cdot g^{-1}$)	External surface area ($m^2 \cdot g^{-1}$)	Pore volume ($cm^3 \cdot g^{-1}$)	Micropore volume ($cm^3 \cdot g^{-1}$)	External pore volume ($cm^3 \cdot g^{-1}$)	BJH adsorption average pore diameter (nm)
NC-800	676.47	194.14	452.33	1.69	0.09	1.66	10.46
NC-900	701.38	235.40	465.98	1.62	0.12	1.55	9.23
NC-1000	997.10	422.48	574.60	2.47	0.21	2.32	9.94
NC-1000N	1,136.44	467.60	668.84	2.27	0.24	2.15	8.00
NCS-1000N	1,256.67	643.48	613.18	2.33	0.33	2.04	7.40

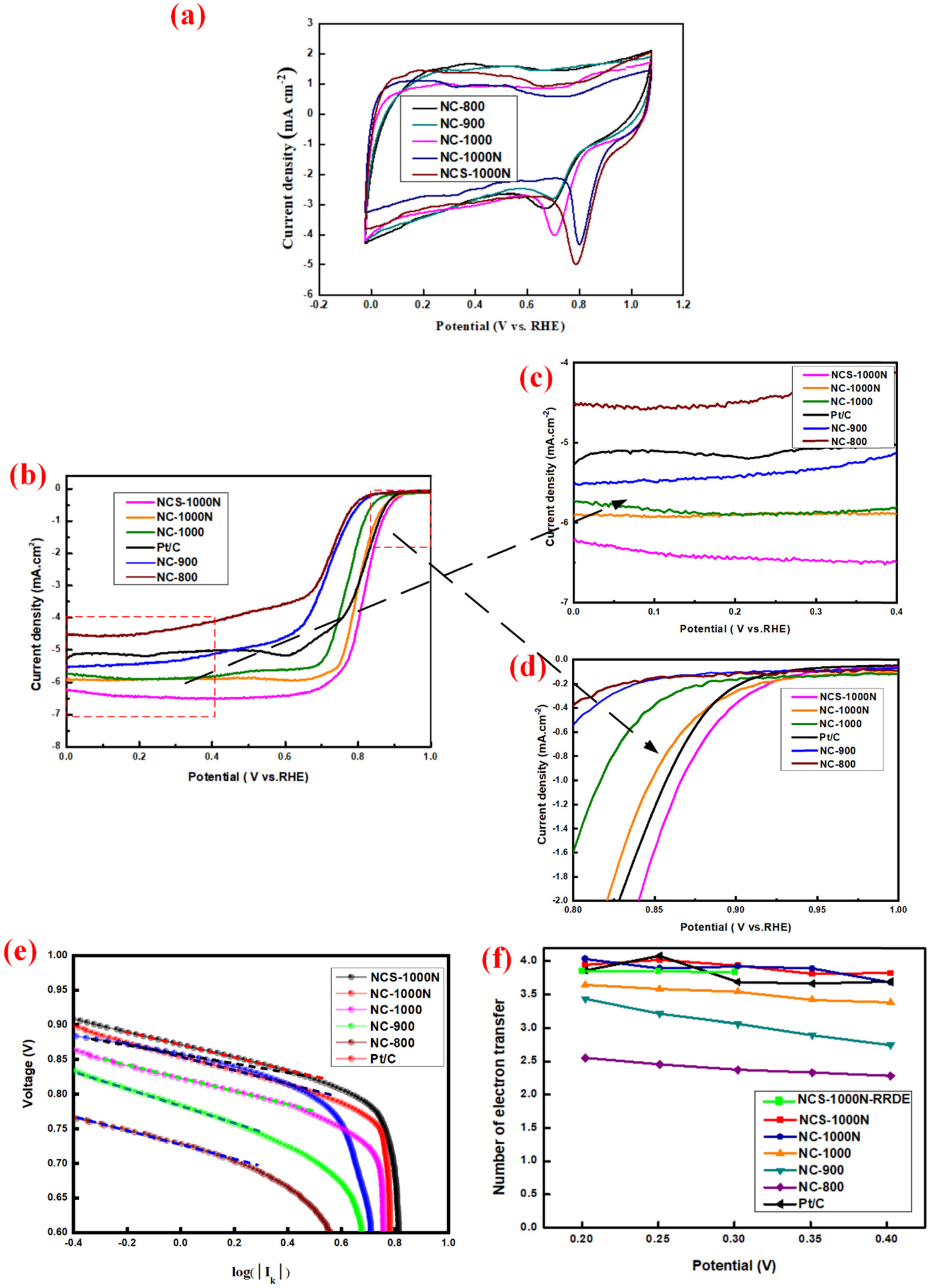

Figure 8: (a) CV cycles recorded in O_2-saturated solution. (b)–(d) LSVs recorded in an O_2-saturated 0.1 M KOH with a scan rate of 5 mV·s^{-1}and 1,600 rpm. (e) Tafel curves. (f) Average number of e-transferred of various NCs.

The XPS results in Section 3.6 reveal that higher calcination temperatures generate more active nitrogen species, such as graphitic-N or pyridinic-N. The LSV results demonstrate that NC-1000 exhibits better catalytic ability, confirming the critical role played by these two active configurations in the ORR. The results indicate that a higher pyrolysis temperature is the key parameter for further experiments.

In Figure 8(b), the LSV curve was used to assess the ORR capabilities of catalysts prepared under different conditions. These catalysts were compared to commercial Pt/C catalysts. Figure 8(c) and Table 3 provide electrochemical parameters for the prepared NC-1000, NC-1000N, and NCS-1000N catalysts in an alkaline environment, and they all exhibit higher LRCDs (NC-1000: −5.73, NC-1000N: −5.92, NCS-1000N: −6.21) compared to Pt/C (−5.30). Furthermore, the half-wave potential for NCS-1000N is even more positive at 0.82 V (Figure 8(d)), indicating that sulfur doping plays a significant role in improving the ORR. It is attributed to the sulfur doping, which increases the defects in planar graphene, thus enhancing the surface area. Additionally, it can modify the spin of material defects and redistribute charge density, promoting oxygen adsorption and the synergic effect between nitrogen and sulfur, ultimately increasing the density of active sites and improving electrochemical performance.

Moreover, all the catalysts in this experiment have excellent surface areas, highlighting the importance of a high surface area in preparing highly active non-metallic catalysts. Among them, NC-1000N exhibits more positive $E_{1/2}$, a more negative LRCD, and a higher E_{onset} than NC-1000. It demonstrates the successful strategy of using NH_4Cl for assisted calcination, as NH_4Cl generates NH_3, modifying the number of micropores in the material to facilitate the formation of a catalytically friendly layered porous structure. These porous, reticulated channels increase the exposure of active sites, enabling gases and electrolytes to enter for the ORR catalysis. The results suggest that the catalyst NCS-1000N is particularly promising, showcasing the significance of sulfur doping and NH_4Cl-assisted calcination in enhancing the ORR catalytic performance.

In an alkaline environment, the Tafel slopes for the NC-1000N and NCS-1000N (Figure 8(e)) catalysts are 96.1 and 87.6 mV·dec^{-1}, respectively, which are close to the Tafel slope of 75.5 mV·dec^{-1} for commercial Pt/C. It confirms that the catalyst materials synthesized in this experiment exhibit a rate-determining step comparable to commercial Pt/C, and it also validates the high electrical conductivity of the materials mentioned in Section 3.5.

3.8.3 Electron transfer number

Based on the LSV results, the catalysts NC-1000N and NCS-1000N, which exhibited superior oxygen reduction performance, were further investigated by recording ORR polarization curves at varying rotation speeds (400–2,500 rpm) in O_2-saturated 0.1 M KOH solution. As illustrated in Figure S12, increasing the rotation speed leads to a corresponding increase in current density. This enhancement arises from a reduced diffusion layer thickness between the RDE and the bulk electrolyte, accelerating oxygen mass transport and increasing the diffusion-limited current.

To gain deeper insights into the ORR kinetics, current densities within the potential range of 0.4 V–0.2 V (vs RHE) were used to construct Koutecky–Levich (K–L) plots. The slopes of the K–L plots were applied to the K–L equation to determine the average number of electrons transferred per oxygen molecule (*n*). The results reveal that NC-1000N exhibits an average electron transfer number of approximately 4.0, while NCS-1000N demonstrates an average of 3.9. These values are close to the theoretical maximum of four electrons, indicating that both catalysts predominantly follow a four-electron ORR pathway, effectively reducing O_2 to OH^- and suppressing the formation of peroxide intermediates (HO_2^-).

Additionally, the influence of calcination temperature on electron transfer behavior was examined (Figure 8f). The data show that the average electron transfer number increases with increasing pyrolysis temperature, indicating improved ORR selectivity toward the 4e$^-$ pathway

Table 3: Electrochemical properties of various NCs and Pt/C

NCs	E_{onset} (V)	$E_{1/2}$ (V)	LRCD (mA·cm^{-2})	Tafel slope (mV·dec^{-2})	Average no. of e-transferred
NC-800	0.77	0.71	−4.54	143.0	2.4
NC-900	0.82	0.71	−5.54	135.6	3.1
NC-1000	0.83	0.77	−5.73	96.3	3.5
NC-1000N	0.94	0.80	−5.92	96.1	4.0
NCS-1000N	0.96	0.82	−6.21	87.6	3.9
Pt/C	1.00	0.81	−5.30	75.5	3.8

at higher temperatures. The observation agrees with the LSV results and suggests that elevated temperatures promote the formation of more catalytically active nitrogen configurations (e.g., graphitic-N or pyridinic-N), which favor the complete four-electron reduction of oxygen.

3.8.4 Durability testing

Figure 9(a) shows that the NC-1000N and NCS-1000N catalysts prepared in this study exhibit excellent stability. After running for 25,000 s, the current density of both catalysts decreased by less than 2%, while the commercial platinum carbon catalyst experienced a reduction of approximately 15% in the initial current. The experimental results highlight the significant advantages of non-metal nitrogen-doped materials. The absence of precious metals eliminates the issue of carbon monoxide poisoning, and it also avoids performance degradation due to metal corrosion during operation. As a result, the non-metal catalyst materials in this study demonstrate much better ORR durability than commercial Pt/C, with NCS-1000N retaining 99% of its initial current density. This high level of stability indicates the potential for practical commercial applications.

The results in Figure 9(b) indicate that the commercial Pt/C catalyst is significantly affected by methanol poisoning, as it rapidly deactivates after methanol introduction. In contrast, the NC-1000N and NCS-1000N catalysts in this study maintain stable current values and remain unaffected by methanol poisoning. It demonstrates that the non-metal catalysts in this study have excellent methanol tolerance.

3.9 Single-cell testing

Figure 10 displays the results of single fuel cell polarization tests at different temperatures and the OCV, max. power density ($P_{\max}$) and max. The current density ($I_{\max}$) of cells with various types of cathode catalysts is listed in Table 4. As mentioned, catalysts with higher calcination temperatures possess favorable catalytic factors such as higher specific surface area, high conductivity, and enhanced ORR activity. Consequently, the single fuel cell polarization testing results show that the current density and $P_{\max}$s of the MEA increase as the catalyst calcination temperature rises. These results align with the trends observed in the LSV tests. In particular, the NC-1000 catalyst exhibits superior current density compared to NC-800 and NC-900, highlighting the catalyst's high mass transport capability and an impressive maximum power density of 333.2 mW·cm^{-2}.

The results for the three non-metallic materials synthesized in this experiment consistently outperform the commercial Pt/C catalyst in current density and maximum power density, highlighting their practical application value. NC-1000N, prepared using NH_4Cl as a pore-forming agent, exhibits a layered porous material with micro-mesoporous channels. This configuration accelerates mass transport, improving NC-1000N's Ohmic polarization and concentration polarization, and the power density is significantly superior to that of the NC-1000 catalyst. In contrast, N, S co-doped NCS-1000N presents milder activation polarization, making the reaction easier. The OCV of NCS-1000N is approximately 0.96 V, close to Pt/C's 1.0 V, consistent with LSV results. The exceptional fuel cell

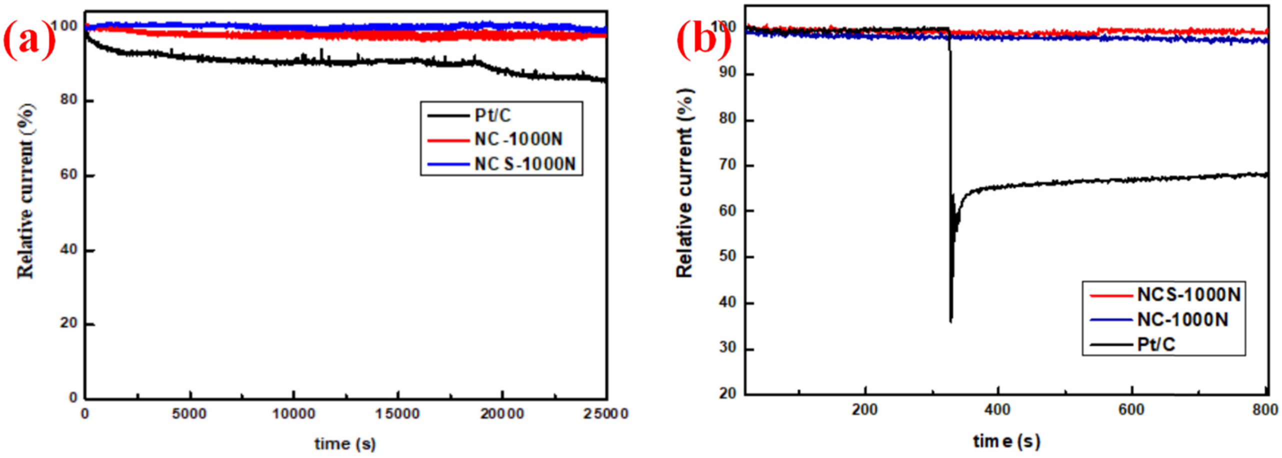

Figure 9: (a) The current–time (*I*–*t*) chronoamperometric response of ORR at NC-1000N, NCS-1000N, and Pt/C electrodes in O_2-saturated 0.1 M KOH solution with the rotation rate of 1,200 rpm at a bias voltage of 0.4 V (vs RHE). (b) Chronoamperometric responses on injection of CH_3OH at t = 300 s (1,600 rpm in O_2-saturated aqueous electrolyte).

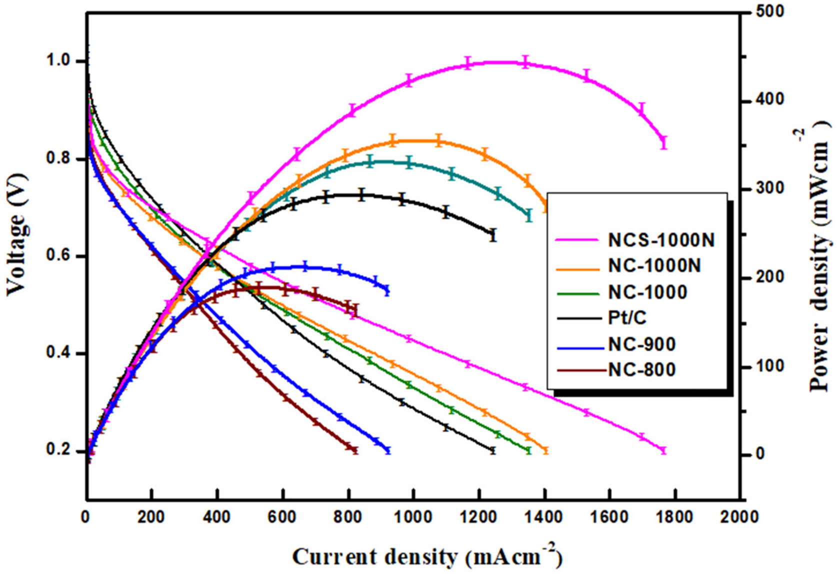

Figure 10: Single-cell polarization curves of various NCs and commercial Pt/C cathode catalysts.

Table 4: Properties of cells with Pt/C and various NC cathode catalysts

Cathode	Anode	OCV (V)	P_{max} (mW cm^{-2})	I_{max} (mA cm^{-2})
Pt/C	Pt/C	1.0	295.2	1,244.0
NC-800	Pt/C	0.86	190.1	822.5
NC-900	Pt/C	0.87	213.9	921.1
NC-1000	Pt/C	0.93	333.2	1,351.3
NC-1000N	Pt/C	0.94	357.2	1,407.0
NCS-1000N	Pt/C	0.96	443.8	1,756.9

performance is attributed to sulfur doping, which increases defects and enhances the specific surface area. As a result, the NCS-1000N catalyst achieves a P_{max} of 443.0 mW·cm^{-2}, surpassing Pt/C by approximately 147.8 mW·cm^{-2} under the same loading conditions. The comparison of the single-cell performance with other metal-free cathode catalysts is listed in Table S4. This work demonstrates high P_{max} and OCV for the single cell with cathode catalysts of MFNCCs; only cells with PtRu/C anode catalysts outperform our system in P_{max}.

Combining these results demonstrates the potential of the NC-1000N and NCS-1000N catalysts in the actual AEMFC market, offering higher power density than Pt/C. The nonmetallic catalysts are also cost-effective and eco-friendly as they do not require metals, eliminating the energy consumption and pollution associated with acid washing and secondary pyrolysis. These results suggest that further optimization of the MEA manufacturing process or ionomer ratio may lead to even more significant improvements in the single-cell performance.

4 Conclusions

This study reports a rapid and facile synthetic strategy for fabricating non-metallic, nitrogen–sulfur co-doped aromatic PURs using diamine, diisocyanate, and diisothiocyanate monomers as precursors. Direct polymerization followed by pyrolysis in an inert gas atmosphere yields high-surface-area, defect-rich graphitic carbon materials with excellent electrical conductivity and catalytic activity. The electrochemical performance of these metal-free catalysts rivals that of conventional precious metal-based materials, highlighting their potential as cost-effective alternatives for energy conversion applications.

Morphological analyses via SEM and TEM reveal that increasing the pyrolysis temperature promotes defect formation across the flower-like carbon nanosheets, enhancing the accessibility of active sites. Structural characterizations using XRD and Raman spectroscopy confirm the development of a well-graphitized carbon matrix at elevated temperatures. In addition, the four-point probe and electrochemical measurements demonstrate improved conductivity and reduced ohmic losses at 1,000°C, particularly for the NC-1000N catalyst.

The pore-forming role of NH_4Cl significantly enhances the surface area and microporosity of NC-1000N, achieving a BET-specific surface area of 1,136.44 m^2·g^{-1}, facilitating oxygen transport and access to catalytic sites. XPS analyses indicate that NH_4Cl-assisted pyrolysis promotes the formation of active nitrogen configurations, contributing to high catalytic efficiency. As a result, NC-1000N delivers an impressive LRCD of −5.92 mA·cm^{-2}, while the sulfur co-doped NCS-1000N exhibits a slightly higher LRCD of $-6.12\ \mathrm{mA{\cdot}cm^{-2}}$.

Incorporating sulfur into the carbon lattice introduces additional structural defects and modulates the spin-charge distribution, further improving oxygen adsorption kinetics. Consequently, NCS-1000N achieves a high open-circuit voltage of 0.96 V and a half-wave potential of 0.82 V in alkaline conditions. NC-1000N and NCS-1000N show excellent durability and methanol tolerance, maintaining stable performance over 25,000 s of continuous operation.

Fuel cell single-cell evaluations further confirm the catalysts' potential: NC-1000N delivers a *P*max of $357.2\ \mathrm{mW{\cdot}cm^{-2}}$, while NCS-1000N achieves $443.0\ \mathrm{mW{\cdot}cm^{-2}}$, significantly surpassing that of commercial Pt/C-based MEAs ($295.2\ \mathrm{mW{\cdot}cm^{-2}}$) under comparable loading conditions. These results demonstrate that high-activity, metal-free ORR catalysts can be synthesized through a scalable, environmentally benign process without reliance on noble metals.

This work offers a promising pathway for developing low-cost, high-performance cathode materials for AEMFCs. Further optimization, like fine-tuning the monomer composition, polymerization ratios, or MEA fabrication protocols, may lead to even greater performance enhancements and facilitate broader commercialization of these metal-free catalyst systems.

Acknowledgments: We would also like to thank the National Cheng Kung University Instrument Center for their support with AFM (EM000600), EDS (EM000700), HRTEM (EM000800 & EM000900), XRD (XRD005100), XPS (ESCA000200 & ESCA003700), 500 MHz NMR (NMR005000), and TOF-Mass (MS000400) measurements. The funding bodies had no involvement in the collection, analysis, and interpretation of data, nor in the writing of the report or the decision to submit the article for publication. The authors thank Kuang-Kuo Wang at National Sun Yat-sen University for assistance with TEM experiments. The Talos F200X G2 TEM (ID: EM025600) analysis was conducted at the Joint Center of High Valued Instruments, National Sun Yat-sen University.

Funding information: This work was supported by the National Science and Technology Council (NSTC) of Taiwan under grants NSTC 114-2622-E-992-089-, NSTC 114-2622-E-992-003-, NSTC 113-2221-E-992-108-, NSTC 113-2622-E-992-004, NSTC 113-2221-1-224-059, NSTC 112-2622-E-992-012-, and NSTC 112-2221-E-992-001-.

Author contributions: Yu-Chang Huang: Writing – review & editing, Methodology; Po-Hao Tseng: Formal Analysis; Yen-Zen Wang: Writing – original draft; Ko-Shan Ho: Writing – review & editing, Methodology; Yan-Cheng Lin: Visualization, Project administration; Che-Ju Tseng: Resources.

Conflict of interest: The authors state no conflict of interest.

Data availability statement: Data available on request from the authors.

References

(1) Marinoiu A, Raceanu M, Carcadea E, Varlam M. Nitrogen-doped graphene oxide as efficient metal-free electrocatalyst in PEM fuel cells. Nanomaterials (Basel). 2023;13(7):1233. doi: 10.3390/nano13071233.

(2) Yaengthip P, Siyasukh A, Payattikul L, Kiatsiriroat T, Punyawudho K. The ORR activity of nitrogen doped-reduced graphene oxide below decomposition temperature cooperated with cobalt prepared by strong electrostatic adsorption technique. J Electroanal Chem. 2022;915:116366. doi: 10.1016/j.jelechem.2022.116366.

(3) Logeshwaran N, Panneerselvam IR, Ramakrishnan S, Kumar RS, Kim AR, Wang Y, et al. Quasihexagonal platinum nanodendrites decorated over CoS_2-N-doped reduced graphene oxide for electro-oxidation of C1-, C2-, and C3-type alcohols. Adv Sci. 2022;9(8):2105344. doi: 10.1002/advs.202105344.

(4) Skorupska M, Ilnicka A, Lukaszewicz JP. The effect of nitrogen species on the catalytic properties of N-doped graphene. Sci Rep. 2021;11(1):23970. doi: 10.1038/s41598-021-03403-8.

(5) Ganyecz Á, Kállay M. Oxygen reduction reaction on N-doped graphene: Effect of positions and scaling relations of adsorption energies. J Phys Chem C Nanomater Interfaces. 2021;125(16):8551–61. doi: 10.1021/acs.jpcc.0c11340.

(6) Marinoiu A, Carcadea E, Sacca A, Carbone A, Sisu C, Dogaru A, et al. One-step synthesis of graphene supported platinum nanoparticles as electrocatalyst for PEM fuel cells. Int J Hydrogen Energy. 2021;46(22):12242–53. doi: 10.1016/j.ijhydene.2020.04.183.

(7) Marinoiu A, Andrulevicius M, Tamuleviciene A, Tamulevicius T, Raceanu M, Varlam M. Synthesis of well dispersed gold nanoparticles on reduced graphene oxide and application in PEM fuel cells. Appl Surf Sci. 2020;504:144511. doi: 10.1016/j.apsusc.2019.144511.

(8) Hu C, Dai L. Carbon-based metal-free catalysts for electrocatalysis beyond the ORR. Angew Chem Int Ed. 2016;55(39):11736–58. doi: 10.1002/anie.201509982.

(9) Jiang Z, Yu J, Huang T, Sun M. Recent advance on polyaniline or polypyrrole-derived electrocatalysts for oxygen reduction reaction. Polymers. 2018;10(12):1397, https://www.mdpi.com/2073-4360/10/12/1397.

(10) Xing S, Yu X, Wang G, Yu Y, Wang Y, Xing Y. Confined polyaniline derived mesoporous carbon for oxygen reduction reaction. Eur Polym J. 2017;88:1–8. doi: 10.1016/j.eurpolymj.2017.01.011.

(11) Xu J, Lu S, Zhou H, Chen X, Wang Y, Xiao C, et al. A highly efficient electrocatalyst derived from polyaniline@CNTs–SPS for the oxygen reduction reaction. ChemElectroChem. 2018;5(1):195–200. doi: 10.1002/celc.201700735.

(12) An H, Zhang R, Li Z, Zhou L, Shao M, Wei M. Highly efficient metal-free electrocatalysts toward oxygen reduction derived from carbon

nanotubes@polypyrrole core–shell hybrids. J Mater Chem A. 2016;4(46):18008–14. doi: 10.1039/C6TA08892A.

(13) Osmieri L, Monteverde Videla AHA, Specchia S. Optimization of a Fe–N–C electrocatalyst supported on mesoporous carbon functionalized with polypyrrole for oxygen reduction reaction under both alkaline and acidic conditions. Int J Hydrogen Energy. 2016;41(43):19610–28. doi: 10.1016/j.ijhydene.2016.05.270.

(14) Tu K, Zou L, Yang C, Su Y, Lu C, Zhu J, et al. Ionic polyimide derived porous carbon nanosheets as high-efficiency oxygen reduction catalysts for Zn–air batteries. Chem – Eur J. 2020;26(29):6525–34. doi: 10.1002/chem.201904769.

(15) Palm I, Kibena-Põldsepp E, Mooste M, Kozlova J, Käärik M, Kikas A, et al. Nitrogen and sulphur co-doped carbon-based composites as electrocatalysts for the anion-exchange membrane fuel cell cathode. Int J Hydrogen Energy. 2024;55:805–14. doi: 10.1016/j.ijhydene.2023.11.185.

(16) Gong K, Du F, Xia Z, Durstock M, Dai L. Nitrogen-doped carbon nanotube arrays with high electrocatalytic activity for oxygen reduction. Science. 2009;323(5915):760–4. doi: 10.1126/science.1168049.

(17) Fu X, Li N, Ren B, Jiang G, Liu Y, Hassan FM, et al. Tailoring FeN_4 sites with edge enrichment for boosted oxygen reduction performance in proton exchange membrane fuel cell. Adv Energy Mater. 2019;9(11):1803737. doi: 10.1002/aenm.201803737.

(18) Zhang C, Lin S, Peng J, Hong Y, Wang Z, Jin X. Preparation of highly porous carbon through activation of NH4Cl induced hydrothermal microsphere derivation of glucose. RSC Adv. 2017;7(11):6486–91. doi: 10.1039/C6RA26141H.

(19) Rastegar A, Gholami M, Jafari AJ, Hosseini-Bandegharaei A, Kermani M, Hashemi YK. Use of $NH_{(4)}Cl$ for activation of carbon xerogel to prepare a novel efficacious adsorbent for benzene removal from contaminated air streams in a fixed-bed column. J Environ Health Sci Eng. 2020;18(2):1141–9. doi: 10.1007/s40201-020-00533-5.

(20) Hansen GP, Dominguez RJG, Hoppens NC, Shields ES, Bulluck JW. Novel Polyurea Fiber. U.S. patent 2011/0082274 A1.

(21) Wang Y-Z, Huang Y-C, Fu X-Y, Ho K-S. Thermally degraded polyurea as cathode catalyst of an anion exchange membrane fuel cell. Polym Degrad Stab. 2023;217:110540. doi: 10.1016/j.polymdegradstab.2023.110540.

(22) Ketata N. Thermal degradation of polyurethane bicomponent systems in controlled atmospheres. Polym Polym Compos. 2005;13(1):1–26. doi: 10.1177/096739110501300101.

(23) McKenna ST, Hull TR. The fire toxicity of polyurethane foams. Fire Sci Rev. 2016;5(1):3. doi: 10.1186/s40038-016-0012-3.

(24) Zarzyka I, Majda D. Thermogravimetric and qualitative analysis of thermal decomposition characteristics of polyurethane foams based on polyols with carbamide or oxamide and borate groups. Polym Int. 2017;66(11):1675–83. doi: 10.1002/pi.5433.

(25) Gao C, Jin YZ, Kong H, Whitby RLD, Acquah SFA, Chen GY, et al. Polyurea-functionalized multiwalled carbon nanotubes: Synthesis, morphology, and Raman spectroscopy. J Phys Chem B. 2005;109(24):11925–32. doi: 10.1021/jp051642h.

(26) Lai Q, Zheng J, Tang Z, Bi D, Zhao J, Liang Y. Optimal configuration of N-doped carbon defects in 2D turbostratic carbon nanomesh for advanced oxygen reduction electrocatalysis. Angew Chem Int Ed. 2020;59(29):11999–2006. doi: 10.1002/anie.202000936.

(27) Huang WY, Jheng LC, Hsieh TH, Ho KS, Wang YZ, Gao YJ, et al. Calcined Co(II)-triethylenetetramine, Co(II)- polyaniline-thiourea as the cathode catalyst of proton exchanged membrane fuel cell. Polymers (Basel). 2020;12(12):3070. doi: 10.3390/polym12123070.

(28) Kuo C-W, Ho K-S, Wang R-Y, Chang J-K, Lin Y-C, Lee P-Y, et al. Synthesis of CoN_xS_y-rGO composites for use as cathode catalysts in anion-exchange membrane fuel cells. Int J Hydrogen Energy. 2025;143:740–50. doi: 10.1016/j.ijhydene.2025.05.108.

(29) Subramanian NP, Li X, Nallathambi V, Kumaraguru SP, Colon-Mercado H, Wu G, et al. Nitrogen-modified carbon-based catalysts for oxygen reduction reaction in polymer electrolyte membrane fuel cells. J Power Sources. 2009;188(1):38–44. doi: 10.1016/j.jpowsour.2008.11.087.

(30) Liu G, Li X, Ganesan P, Popov BN. Studies of oxygen reduction reaction active sites and stability of nitrogen-modified carbon composite catalysts for PEM fuel cells. Electrochim Acta. 2010;55(8):2853–8. doi: 10.1149/1.3210680.

(31) Tian X, Sun X, Jiang Z, Jiang Z-J, Hao X, Shao D, et al. Exploration of the active center structure of nitrogen-doped graphene for control over the growth of Co_3O_4 for a high-performance supercapacitor. ACS Appl Energy Mater. 2018;1(1):143–53. doi: 10.1039/C2EE21802J.

(32) Strelko VV, Kuts VS, Thrower PA. On the mechanism of possible influence of heteroatoms of nitrogen, boron and phosphorus in a carbon matrix on the catalytic activity of carbons in electron transfer reactions. Carbon. 2000;38(10):1499–503. doi: 10.1016/S0008-6223(00)00121-4.

(33) Rao CV, Cabrera CR, Ishikawa Y. In search of the active site in nitrogen-doped carbon nanotube electrodes for the oxygen reduction reaction. J Phys Chem Lett. 2010;1(18):2622–7. doi: 10.1021/jz100971v.

(34) Lin Z, Waller GH, Liu Y, Liu M, Wong C-P. 3D nitrogen-doped graphene prepared by pyrolysis of graphene oxide with polypyrrole for electrocatalysis of oxygen reduction reaction. Nano Energy. 2013;2(2):241–8. doi: 10.1016/j.nanoen.2012.09.002.

(35) Li J-C, Qin X, Hou P-X, Cheng M, Shi C, Liu C, et al. Identification of active sites in nitrogen and sulfur co-doped carbon-based oxygen reduction catalysts. Carbon. 2019;147:303–11. doi: 10.1016/j.carbon.2019.01.018.

(36) Chao G, Zhang L, Wang D, Chen S, Guo H, Xu K, et al. Activation of graphitic nitrogen sites for boosting oxygen reduction. Carbon. 2020;159:611–6. doi: 10.1016/j.carbon.2019.12.052.

(37) Cheng Y, Wang Y, Wang Q, Liao Z, Zhang N, Guo Y, et al. Hierarchically porous metal-free carbon with record high mass activity for oxygen reduction and Zn-air batteries. J Mater Chem A. 2019;7(16):9831–6. doi: 10.1039/C9TA02220A.

(38) Yang Z, Yao Z, Li G, Fang G, Nie H, Liu Z, et al. Sulfur-doped graphene as an efficient metal-free cathode catalyst for oxygen reduction. ACS Nano. 2012;6(1):205–11. doi: 10.1021/nn203393d.

(39) Liang J, Jiao Y, Jaroniec M, Qiao SZ. Sulfur and nitrogen dual-doped mesoporous graphene electrocatalyst for oxygen reduction with synergistically enhanced performance. Angew Chem Int Ed. 2012;51(46):11664–8. doi: 10.1002/anie.201206720.

(40) Jaouen F, Proietti E, Lefèvre M, Chenitz R, Dodelet J-P, Wu G, et al. Recent advances in non-precious metal catalysis for oxygen-reduction reaction in polymer electrolyte fuel cells. Energy Environ Sci. 2011;4(1):114–30. doi: 10.1039/C0EE00011F.

(41) Lee SH, Kim J, Chung DY, Yoo JM, Lee HS, Kim MJ, et al. Design principle of Fe–N–C electrocatalysts: How to optimize multimodal porous structures? J Am Chem Soc. 2019;141(5):2035–45. doi: 10.1021/jacs.8b11129.

(42) Guo J, Li B, Zhang Q, Liu Q, Wang Z, Zhao Y, et al. Highly accessible atomically dispersed Fe-N_x sites electrocatalyst for proton-exchange membrane fuel cell. Adv Sci. 2021;8(5):2002249. doi: 10.1002/advs.202002249.